Characterization and High-Temperature Fretting Wear Resistance of HVOF-Sprayed Cr₃C₂-NiCr, CoCrWC and CoCrWNiC Hardfacing Coatings

Pejman Zamani[1] · Reza Ghasemi[1] · Shahla Torabi[1] · Behta Mirjani[1] ·
Mahmood Memari[1] · Mohammad Alizadeh[1] · Hiwa Khaledi[1]

Abstract In the present study, Cr_3C_2-25wt%NiCr, CoCrWC (Stellite-6) and CoCrWC (FSX 414) coatings were deposited by the high-velocity oxy-fuel process on Hastelloy X substrates. The microstructure of the coatings was characterized using field emission scanning electron microscopy. X-ray diffraction was employed to identify the phase composition of the coatings. Tensile bond strength, elastic modulus and Vickers microhardness of the coatings were measured. A self-mated fretting wear test was also carried out on the coatings at room temperature and 550 °C. The results showed that some carbide dissolution occurred during the formation of Cr_3C_2-NiCr coating, although the coating displayed the highest bonding strength, Vickers microhardness and elastic modulus. The Stellite-6 coating showed a significant amount of unmelted particles and the most surface roughness. Oxide stringers were the main microstructural defect of the FSX 414 coating. The Stellite-6 and Cr_3C_2-NiCr coating had the best fretting wear resistance at the temperature of 25 and 550 °C, respectively. The wear mechanisms of the hardfacing coatings were discussed in detail.

Keywords characterization · fretting wear · hardfacing coatings · HVOF · thermal spray

✉ Pejman Zamani
  Pejmanzamani33@yahoo.com

1 Technology Development Department, Middle East Turbo Compressor Co. (Turbotec), Tehran, Iran

Introduction

Fretting wear is a common damage in the gas turbine industry affecting maintenance, safety and reliability. According to ASTM G40-13, fretting wear is known as a wear mode occurring in small amplitude (typically 20-200 μm) oscillatory contacts between surfaces. Dovetail joints, fir tree joints, fuel nozzles, bullhorns, liner stops, brackets and side seals are the critical parts in gas turbine engines that are prone to fretting wear damage. These parts usually operate at temperatures up to 550 °C. Reducing the thickness of the contact faces will result in increased vibration and gas leakage, thereby reducing the turbine output (Ref 1-5). High-velocity oxy-fuel (HVOF) spraying is one of the thermal spraying techniques used for producing wear-resistant coatings. Some Co-based and carbide-based compositions deposited by the HVOF process have been successfully applied on gas turbine components exposed to fretting wear. There is little information on the fretting wear mechanism of these coatings (Ref 6-8).

Cr_3C_2-based coatings have been thermally sprayed to a wide range of industrial components (Ref 9). The HVOF-sprayed Cr_3C_2-NiCr coatings display significant corrosion and oxidation resistance. In addition, the coatings retain high hardness and wear resistance to operating temperatures up to 900 °C. In a Cr_3C_2-NiCr cermet coating, wear resistance is supplied by the carbide ceramic phase, while the corrosion resistance is basically due to the NiCr alloy phase (Ref 5, 10-12).

CoCrW(Mo)C, as a member of the Co-based hardfacing alloys named Stellite-6, is well known for numerous industrial applications. The microstructure of the Stellite-6 alloy consists of an FCC Co-based matrix including Cr-based carbide phases. The ability to form Cr-based oxide layers imparts good resistance to this alloy against high-

temperature oxidation. Stellite-6 coatings deposited by plasma transferred arc welding, cold spraying and HVOF process show the best performance in the range of 500-850 °C due to the formation of a glaze tribo-film (Ref 13-17).

The CoCrW(Mo)Ni(Fe)C alloy named FSX 414 has been developed by General Electric Company. It has a moderate rupture strength and significant resistance to hot corrosion and oxidation. The chemical composition of the FSX-414 alloy is similar to that of the Stellite 31 alloy, which is capable of forming glaze tribo-films at high temperatures. This alloy, which is commonly available in cast-in bulk, can be used as the preferred option for producing first and, sometimes, second-stage blades in the GE turbines (Ref 11, 18).

Although various companies have produced FSX 414 thermal spray powders, no information is available on the properties of the FSX 414 coating. The present study represents one of the first reports on the characterization of the FSX 414 coating. Besides, comparable data on the properties of the above-mentioned hardfacing coatings are limited.

The ability to fully characterize the microstructural features, mechanical properties and fretting wear performance of the coatings is of paramount importance to understand the in-service properties and eventual selection of the right coatings. In the present work, Cr_3C_2-25wt%NiCr, Stellite-6 and FSX 414 coatings were applied on Hastelloy X by the HVOF spraying and their phase composition, microstructure, mechanical properties and fretting wear performance at temperatures of 25 and 550 °C were characterized as well.

Experimental Procedure

Materials and preparation

Commercially available GTV80.81.1 (Cr_3C_2-25wt%NiCr, agglomerated and sintered), GTV 85.06.1 (Stellite-6, gas atomized) and PAC 8106 (FSX 414, gas atomized) powders were used as the feedstock. The chemical composition and size distribution of the primary powders are presented in Table 1. The morphology of the powders is shown in Fig. 1. The powders are spherical in shape and have a size distribution (11-45 μm) suitable for HVOF spraying. Co-based and Cr_3C_2-NiCr powders were manufactured by gas

atomization and agglomeration and sintering processes, respectively. Therefore, the difference in surface morphology among the powders observed in Fig. 1 is due to their different manufacturing processes.

JP-5000 liquid-fuel HVOF spraying system was employed to deposit the coatings onto degreased and grit blasted Hastelloy X substrates (15 cm × 2 cm × 2 mm). The HVOF spraying parameters were selected, according to Table 2.

Microstructure and Phase Analysis

The microstructure of the coatings was characterized by a field emission scanning electron microscope (FESEM) equipped with an energy-dispersive spectrometer (EDS) (Tescan, MIRA3). The amount of porosities in the coatings was calculated by analyzing the microscopic images (Ref 19). Also, roughness of the as-sprayed coatings was determined by the stylus profilometer (Mitutoyo, SJ-201). The average roughness (Ra) was reported based on the cutoff of 0.8 mm.

X-ray diffraction (XRD) using a Phillips x-ray diffractometer (PW3710) was used to analyze the phase composition of primary powders and their corresponding as-sprayed coatings. The XRD patterns were acquired in the 2θ range from 10° to 90° and at a scanning rate of 0.04°min^{-1}.

Mechanical Properties Measurements

After being grit blasted and glued, bonding strength measurement was performed following the ASTM C633-01 standard test method. For the bonding strength test, AISI 420 steel cylinders with dimensions of Ø 25 mm × 50 mm were prepared. To assure reproducibility of the results, the mean value of four samples was evaluated for each coating set. A high-performance adhesive glue (3M Scotch-weld, SW 2214, USA, minimum bond strength of 70 MPa) was used to join the two specimens, preventing impregnation of the coating and its potential influence on the bonding result. The specimen was placed in the oven at 150 °C for one hour. After these steps, the coated samples were subjected to tensile force using a Zwick & Roell (60 ton) machine with a crosshead loading rate of 1 mm/min, and the bonding strength was obtained by dividing the maximum force by the cross-sectional area of the samples.

Table 1 Chemical composition (wt.%) and size distribution (μm) of feedstock powders

Product	Material Composition	Cr	Co	Ni	C	W	Si	Size distribution
GTV80.81.1	Cr_3C_2-25wt%NiCr	Balanced		20	10	…	…	15-45
GTV 85.06.1	Stellite-6	28	Balanced	…	1.1	4	…	20-45
PAC 8106	FSX 414	29.5	Balanced	10.5	0.2	7	0.8	11-45

Fig. 1 FESEM images from morphology of applied powders: (a) Cr_3C_2-25wt.%NiCr (GTV80.81.1), (b) Stellite-6 (GTV 85.06.1), (c) FSX 414 (PAC 8106)
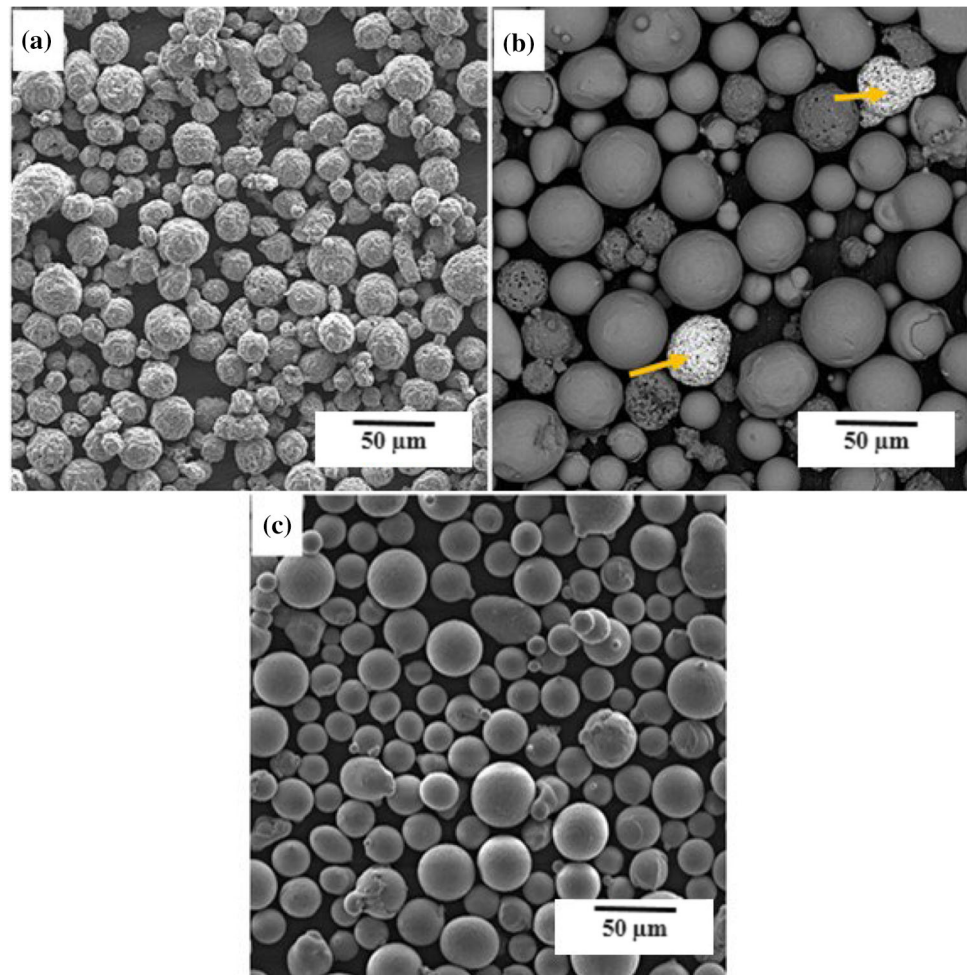
Table 2 Optimized HVOF spraying parameters for the hardfacing coatings

Variables	Cr_3C_2-25wt%NiCr	Stellite-6	FSX-414
Fuel* flow rate (l/hr.)	28	25	28
O_2 flow rate (l/min)	900	960	900
Distance (cm)	33	35	35
Chamber pressure (bar)	8.3-8.5	8.6	8.6
Torch speed (m/s)	0.5	0.5	0.5

*Kerosene ($C_{12}H_{26}$)

Vickers microhardness was measured using a microhardness tester (OGAWA SEIKI CO., LTD). The indentations with a 300 g load were applied near the centerline on the polished cross section of the coatings. The microhardness value ($HV_{0.3}$) of each coating was obtained as the average of five measurements.

There are various methods for determining the elastic modulus of thermal spray coatings based on bending techniques or different types of indentation tests (Ref [20]). In this report, the Knoop hardness method was used to measure the

elastic modulus (E) of the coatings. This method was based on the measurement of the elastic recovery of the surface effect of the indentation diagonals created by the Knoop indenter. Elastic recovery is independent of force and could be correlated with the hardness of coating (H), according to Eq. (1). For this purpose, a 300 g load was applied to the polished cross section of the coating by a Knoop indenter. The diameters of the small (b') and large (a') diagonal were measured by optical microscopy.

$$\frac{b'}{a'} = \frac{b}{a} - \alpha \frac{H}{E} \qquad (Eq\ 1)$$

In this equation, b/a = 0.141 and α = 0.45 (Ref [21]).

Fretting Wear Test

A custom test machine has been designed to evaluate the fretting wear performance of the hardfacing coatings in conditions close to gas turbine operation. Contact surfaces can be placed in a high-temperature furnace. The mentioned fretting wear machine can operate at a frequency of 1-25 Hz and displacement amplitude of 100-1000 μm. As

shown in Fig. 2, the tribo-system includes a vibrator or shaker (1), heating chamber (2), coated sample and mating part holders (3) and weight loading system (4). The coatings were applied on rectangular Hastelloy X substrates with dimensions of $70 \times 20 \times 5$ mm. The mating part with the same coating and same dimensions was selected. Vingsbo and Soderberg (Ref 22) divided the fretting wear conditions into four different regimes, i.e., the reciprocating regime, the gross-slip regime, the mixed stick-slip regime and the stick regime. Given that the contact surfaces in the gas turbine operating in the gross-slip regime, an amplitude of 200 μm was selected. The cycles of fretting wear were chosen to be 360000. Fretting wear test details are given in Table 3.

Before the wear tests, as-deposited specimens were degreased with an ultrasonic bath using acetone for 20 min at 30 kHz. Then, test specimens were weighed with a balance with a sensitivity of 0.0001 g. The test device was heated by the furnace for approximately 2 hours until the desired temperature was reached. K-type thermocouples were used to measure the temperature of the test specimens. After the tests, specimens were cooled down in the furnace and then cleaned and weighed. In this study, weight losses were obtained from the average of three tests on each specimen under the same fretting wear conditions. The volume loss of the coatings was calculated by dividing weight loss per density. The wear scars were also analyzed using FESEM.

Results and Discussion

Microstructure

The polished cross sections of Cr_3C_2-NiCr, Stellite-6 and FSX 414 coatings are shown in Fig. 3. The thickness values of the coatings were 260 ± 30, 280 ± 30 and 180 ± 30 μm,

respectively. The coatings were dense without any cracks or discontinuity, indicating that the HVOF parameters were selected correctly. Retained grits from blasting are observed in the interface between coating and substrate. The porosities of Cr_3C_2-NiCr, Stellite-6 and FSX 414 coatings were measured as 0.9 , 2 and 0.5 %, respectively. The surface roughness of as-sprayed Cr_3C_2-NiCr, Stellite-6 and FSX 414 coatings (R_a) was 4.1, 6.8 and 5.3 μm, respectively. The coating surface roughness was due to the varying degree of the flattening of the heated particles when they impacted the substrate surface. The coatings revealed different degrees of splat flattening. The thermal history of particles strongly affected the degree of splat flattening. The thermal history defined by spraying parameters determines the fractions of melted, partially melted and unmelted particles passed through the HVOF flame (Ref 23, 24).

As shown in Fig. 4(a), different grayscale levels appeared in the backscattered cross section images of the Cr_3C_2-NiCr coating, indicating the presence of different phases in the coating. In this image, the arrangement of the splats and different phases was seen. Based on the principles of the HVOF spraying, the process uses the combustion energy to partially melt and throw the high-speed powder particles (up to 1000 m/s) onto the substrate. The

Table 3 Fretting wear test conditions

| Parameter	Value
Temperature (°C)	25 and 550
Flat displacement amplitude (μm)	200
Cycle length (μm)	400
No. of cycle	3.6×10^5
Accumulated Distance (mm)	144000
Normal force (N)	70
Frequency (Hz)	5
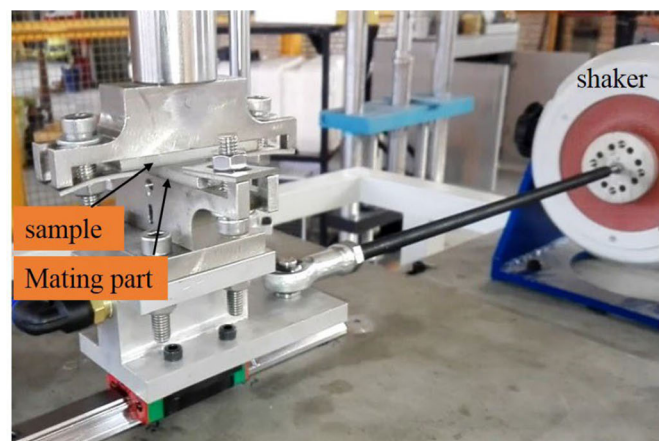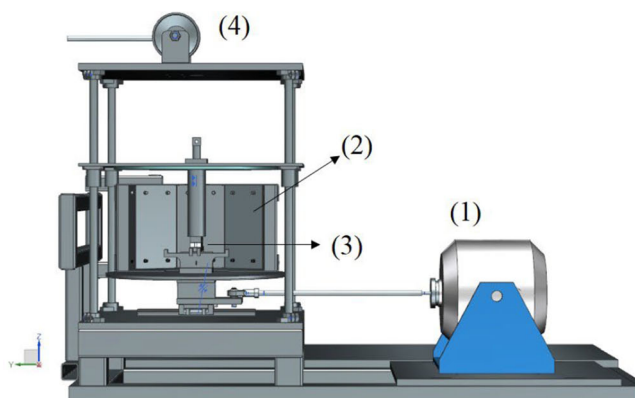
**Fig. 2** Schematic and photograph of the fretting wear machine

heated particles impacted the surface of the substrate that had already been roughened. These particles were flattened by the impact force and quenched at a significant cooling rate (10^6 K/s) (Ref [23]). This high cooling rate was due to the large difference in the substrate and the particle temperatures. Subsequently, the next particles were continuously deposited on previously solidified particles, forming a layer-by-layer coating with a splat morphology (Ref [24]).
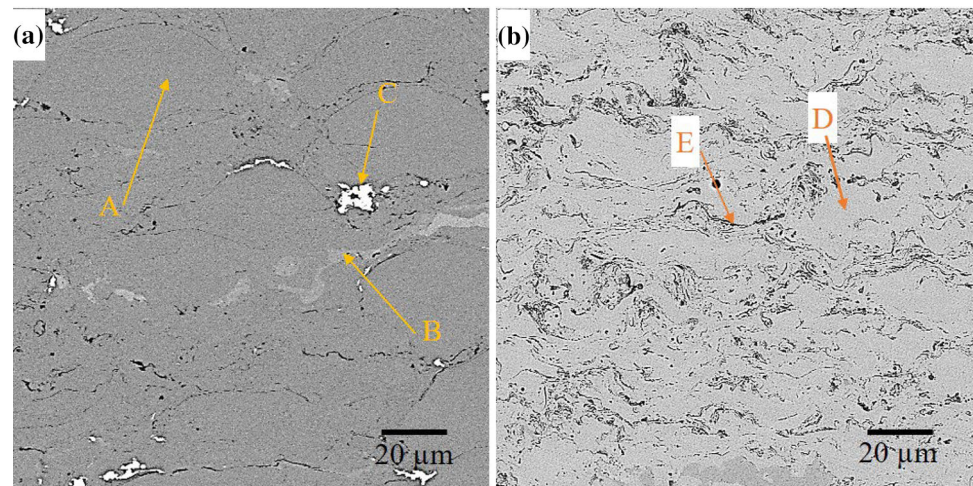

Fig. 3 Polished cross section microstructure of the hardfacing coatings: (a) Cr_3C_2-25wt%NiCr, (b) Stellite-6, (c) FSX 414
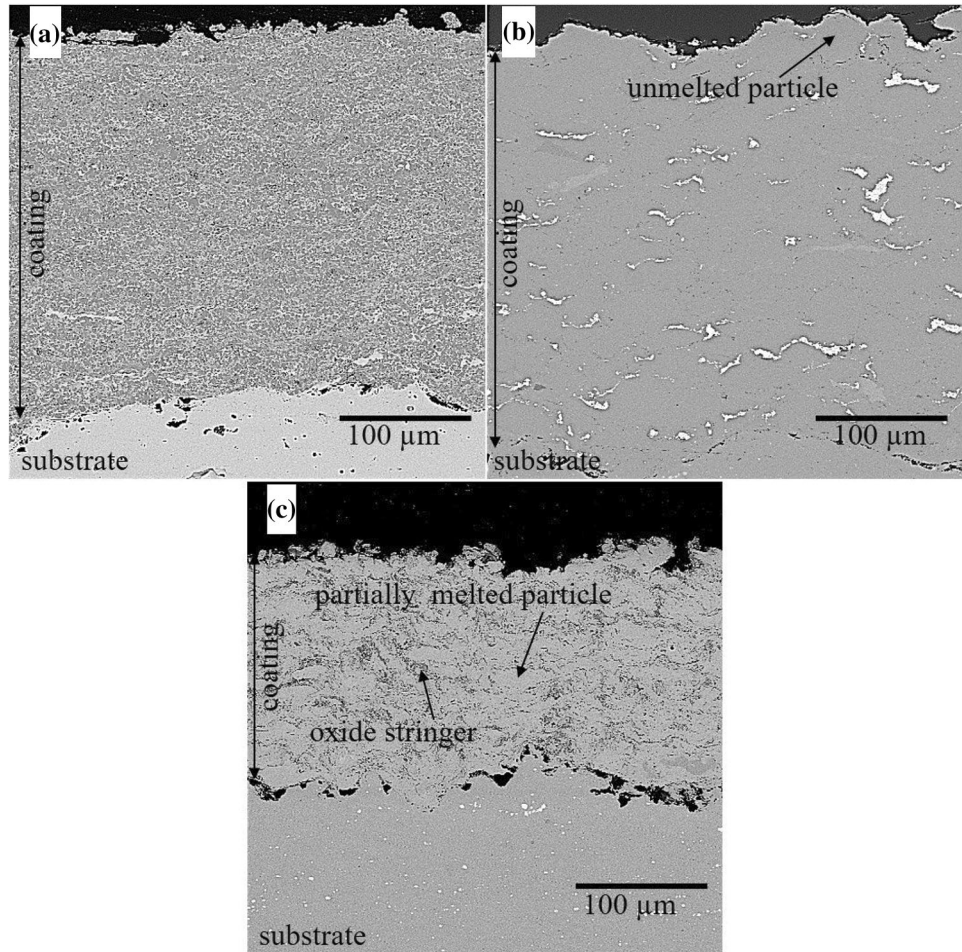
Fig. 4 (a) Backscattered images of the polished cross section of Cr_3C_2-25wt.%NiCr coating, (b) higher magnification of (a)
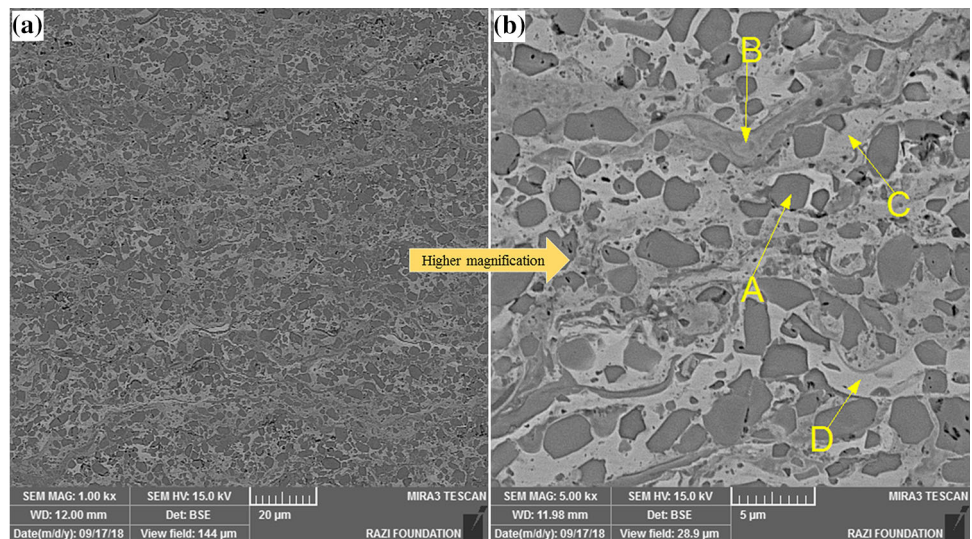
Fig. 5 Backscattered images of the polished cross section of Co-based coatings: (a) Stellite-6 and (b) FSX 414

As can be seen in Fig. 4(b), (a) structure with a mixture of melted (well-flattened) and unmelted particles is observed. The primary Cr_3C_2- NiCr particles were susceptible to carbide dissolution in the NiCr alloy during thermal spraying. This phenomenon changes the carbide content and creates a wide variability of the Cr content in the NiCr alloy (Ref 25). The rapid cooling of the thermal spraying process confined this microstructural and composite disorder to the coating. It means that impact-quenching results in the formation of a metastable, super-saturated solid solution in the Cr,C-enriched matrix. To determine the composition of the different phases in the coating, EDS analysis was carried out. In Fig. 4(b), Point A, with Cr, C, O and Ni elements being 69.2, 22.4, 7.6 and 0.8 in terms of weight percentage (wt.%), suggested that the dark phases in the coating were chromium carbide particles. Point B corresponded to the dark gray phases; it was composed of Cr, Ni, C and O elements with the weight percentages of 41.7, 26.9, 24.0 and 7.4, respectively. Point C, which corresponded to the light gray phases, consisted of Cr, Ni, C and O elements with 36.6, 33.1, 26.5 and 3.8 wt.%, respectively.

The D point, corresponding to the light phases, included Ni, Cr, C and O elements with the weight of 40.6, 30.0, 26.2 and 3.2%, respectively. This indicated that the light phases in the coating were NiCr metal phases, which, due to the lower melting point in comparison with the carbide phases, experienced sufficient temperature to melt and could be, therefore, flattened well after the surface collision.

Analysis of points B and C showed that carbide dissolution occurred in the coating due to non-equilibrium solidification conditions. There was no opportunity to separate carbide and metal phases, resulting in unstable dissolved phases. It means that, due to the rapid solidification, there was no time for carbides to precipitate

from the Cr,C-saturated matrix. The carbide dissolution phenomenon has been previously demonstrated by Matthews et al. (Ref 26) in detailed research agreeing with the present study.

The backscattered images from the cross section of Co-based coatings are presented in Fig. 5. The structure of the Stellite-6 coating revealed more unmelted particles and pores, in contrast to the FSX 414 coating. The splat flattening and the coating density of FSX 414 coating were higher due to its higher fuel flow (28 l/hr) than Stellite-6 (25 l/hr). However, there were more oxide stringers in the FSX 414 coating. The oxidation of particles could occur inside the flame by excess oxygen over the stoichiometry or out of the flame when the particles fly and react with the atmosphere. The oxide phases may affect the cohesive strength of the coating, causing coating delamination when exposed to wear (Ref 21).

As shown in Fig. 5(a), three different phases could be observed in the Stellite-6 coating structure. The background phase (point A) contained Co, Cr, W, C and O elements at 51.5, 23.6, 13.3, 8.8 and 2.8 wt.%, respectively. Point B was a phase containing 18.8, 25, 29.8, 13.7 and 6.2 wt.% Co, Cr, W, C and O elements, respectively. Point C was mainly composed of tungsten, carbon and cobalt due to the impurity of the primary powder (specified in Fig. 1b).

Based on the above results, the background phase in Fig. 5(a) is a cobalt-based solid solution with a slight fluctuation in the concentration of the elements due to the rapid and non-equilibrium cooling of its various regions. Due to the limitations of the EDS method in the quantification of oxygen and carbon elements, the numerical values of the other elements have been somewhat overshadowed. However, the amount of tungsten was significantly higher than the nominal composition. The fluctuation of chemical composition in a melted droplet could affect its solidification behavior, and this could play a role

in the formation of particles with incomplete melting. The presence of carbon and the absence of chromium and tungsten carbides in the background phase indicated that chromium and tungsten carbides were dissolved in the melted droplet and not segregated due to the high cooling rate. This supersaturation of carbides could lead to the deposition of new carbides during high-temperature service and may create a secondary hardening that could be useful, depending on the dominant wear mechanism (Ref 27).

It has been shown that composite coatings containing 15-45 wt.% WC-Co cermet have better behavior in terms of hardness and adhesion strength than the non-cermet containing alloy (Ref 28). Thus, the incorporation of this impurity phase has no adverse effect on the performance of the Stellite-6 coating.

EDS analysis of D and E points specified in Fig. 5(b) was also done. The FSX 414 coating showed two light and dark phases. Point D contained Co, Cr, W, Ni, Fe, C and O elements, with 42.6, 23.7, 11.2, 8.3, 0.7, 9.8 and 3.7 wt.%, respectively. Point E showed black (oxide) stringers rich in chromium (34.3 wt.%) and oxygen (30.3 wt.%). Cobalt, tungsten, nickel and carbon were also present in 6.6, 5.9, 0.7 and 22.2 wt.%.

EDS analysis confirmed that oxide stringers were mainly chromium oxide. The excessive oxidation of the

chromium element during spraying could affect the high-temperature oxidation behavior of the FSX 414 coating.

Phase Composition

The XRD analysis of the as-sprayed Cr_3C_2-NiCr, Stellite-6 and FSX 414 hardfacing coatings is presented in Fig. 6, 7 and 8, respectively. The only detectable crystalline phases in the cermet coating were NiCr and Cr_3C_2 (Fig. 6). However, small amounts of Cr_7C_3 were also identified, too low to be resolved from other overlapping peaks. Most likely, Cr_7C_3 is formed by Cr_3C_2 decarburization. Zimmermann and Kreye (Ref 29) stated that the existence of Cr_7C_3 in the Cr_3C_2-NiCr coating cannot be confirmed by the XRD analysis because its diffraction peaks overlap with the peaks belonging to the Cr_3C_2 and NiCr. In addition, as the cermet coating is thermally sprayed in an oxidizing condition, Cr_3C_2 decarburization appears to be attributed to oxidation of Cr_3C_2 and heating of the primary particles. All peaks were particularly wide at an angle of 43°, indicating the formation of an amorphous/nanostructured or crystalline supersaturated solid solution. The carbide dissolution in the alloy phase and the creation of a NiCr alloy supersaturated in C and Cr could lead to an amorphous field in the low-angle area of the NiCr peak in
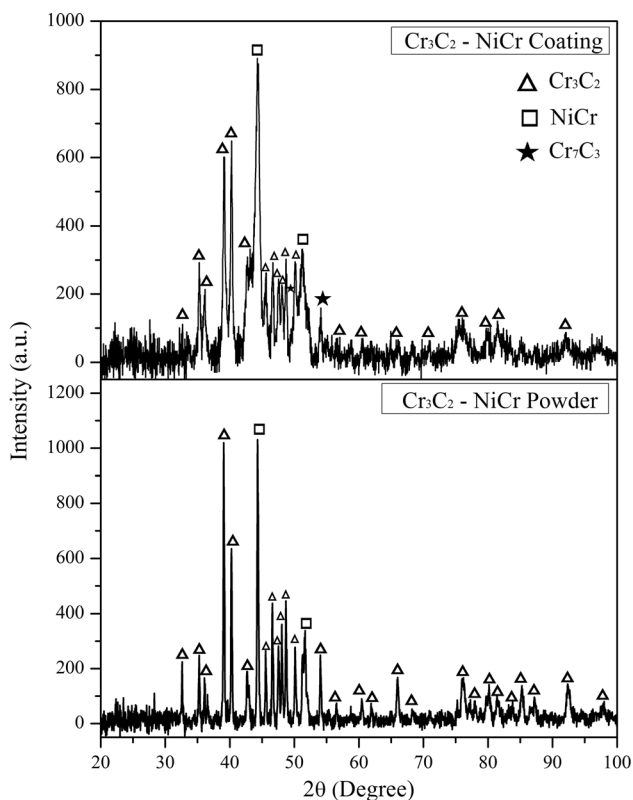
Fig. 6 XRD patterns of the Cr_3C_2-25wt.%NiCr primary powder and corresponding coating
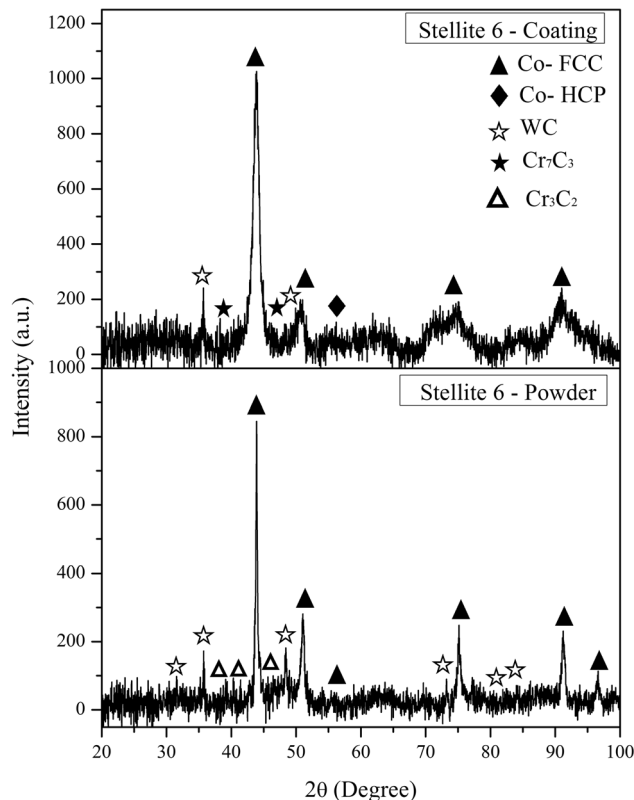
Fig. 7 XRD patterns of the Stellite-6 primary powder and corresponding coating
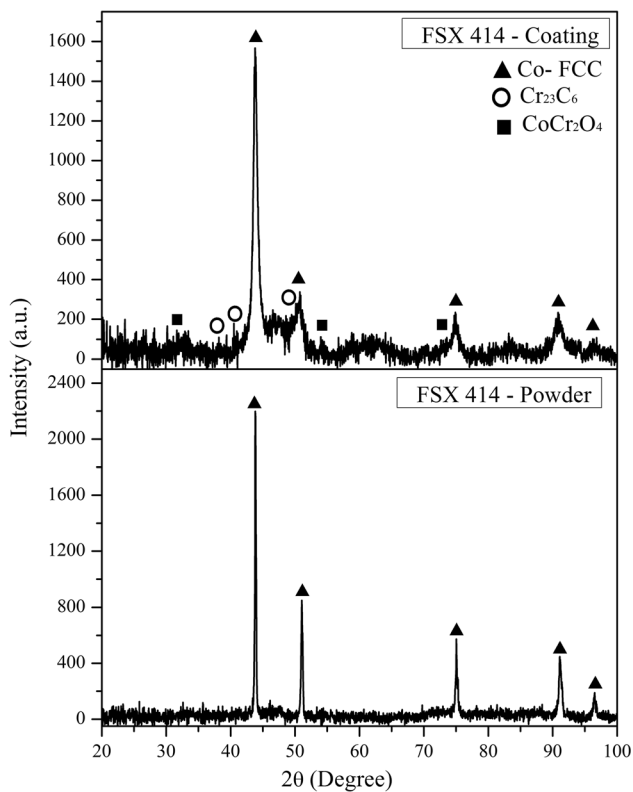
Fig. 8 XRD patterns of the FSX 414 primary powder and corresponding coating

the XRD pattern (Ref 30). BSE images from the cross section of the Cr_3C_2-NiCr coating showed that a large amount of carbide dissolution occurred in the NiCr alloy, which resulted in a decrease in the carbide volume fraction (Fig. 4). The remaining carbide grains were likely to be present in the center of the larger splats. Therefore, microscopic observations and phase composition analysis were in agreement with each other.

The cobalt-based solid solution with FCC structure was identified as the main phase in the Stellite-6 coating (Fig. 7). The other phase observed in the pattern was the tungsten carbide phase. As shown in the microscopic image of the primary powder and the microstructure of the coating, tungsten carbide was impurity in the primary powder. The presence of the Cr_7C_3 phase in the diffraction pattern seemed likely. The HCP structure of the cobalt solid solution was also detectable. This phase was partially formed during the coating process. The presence of oxide and other phases in the diffraction pattern could not be verified.

Co-FCC solid solution phase was identified as the main phase in the XRD pattern of the FSX 414 coating (Fig. 8). Some of the peaks could be related to $Cr_{23}C_6$ and $CoCr_2O_4$ phases. As observed in the microscopic images, the coating contained significant oxide stringers resulting from the oxidation of melted particles during the coating process.

Mechanical Properties

Tensile Bond Strength

The fracture surface images of the coatings after the pull-off test are given in Fig. 9. The failure of chromium carbide, Stellite-6 and FSX 414 coatings occurred in the glue, inside the coating and in the substrate–coating interface, respectively. The average bond strength values for chromium carbide, Stellite-6 and FSX 414 coatings were more than 70±4, 54±3 and 59±4 MPa, respectively. As a result, the Cr_3C_2-NiCr coating had the highest bond strength. Many researchers have attributed the adhesion of thermally sprayed coatings to the surface of components based on a mechanical interlocking mechanism (Ref 23, 24, 31).

The observed difference in the bond strength of the coatings could be related to the crack propagation characteristics. The cracks in the coating tended to propagate along the weak paths, such as splat boundaries. Crack propagation is difficult when good wetting between two layers (splat–splat or splat–substrate) is achieved; thus, stress is required to separate the layers, and hence, the cohesive strength within the coating is increased. As observed in the Stellite-6 microscopy (Fig. 5a), the microstructure of the coating contained large amounts of unmelted particles, indicating that the temperature or velocity of the particles was not high enough when they impacted the substrate surface. There were also some pores between the splats. Both of these factors weakened the bonding strength of the coating. Stellite-6 coating failure in the pull-off test occurred within the coating (Fig. 9b, cohesive failure). The microscopic image of the FSX 414 coating (Fig. 5b) also revealed that the splats of the coatings had a high degree of flattening and wetting. Therefore, cracks required more energy to propagate among the splats, resulting in higher bond strength. In this coating, the weakest area was the interface between the coating and the substrate. As a result, the FSX 414 coating failure occurred along the interface (Fig. 9c, adhesive failure). In the case of the chromium carbide coating, during the tensile test, failure in the glue occurred. This indicated that the coating strength was higher than the nominal glue strength (>70 MPa).

Vickers Microhardness

Hardness is a crucial factor influencing the wear performance of thermally sprayed coatings. According to the well-known Archard equation (Ref 32), higher surface hardness results in higher wear resistance. Vickers microhardness values from the polished cross section of chromium carbide, Stellite-6 and FSX 414 coatings are given in Table 4. The average values were 939, 610 and 760 $HV_{0.3}$,

Fig. 9 The fracture surface of as-sprayed coatings after the pull-off test: (a) Cr_3C_2-25wt.%NiCr, (b) Stellite-6, (c) FSX 414
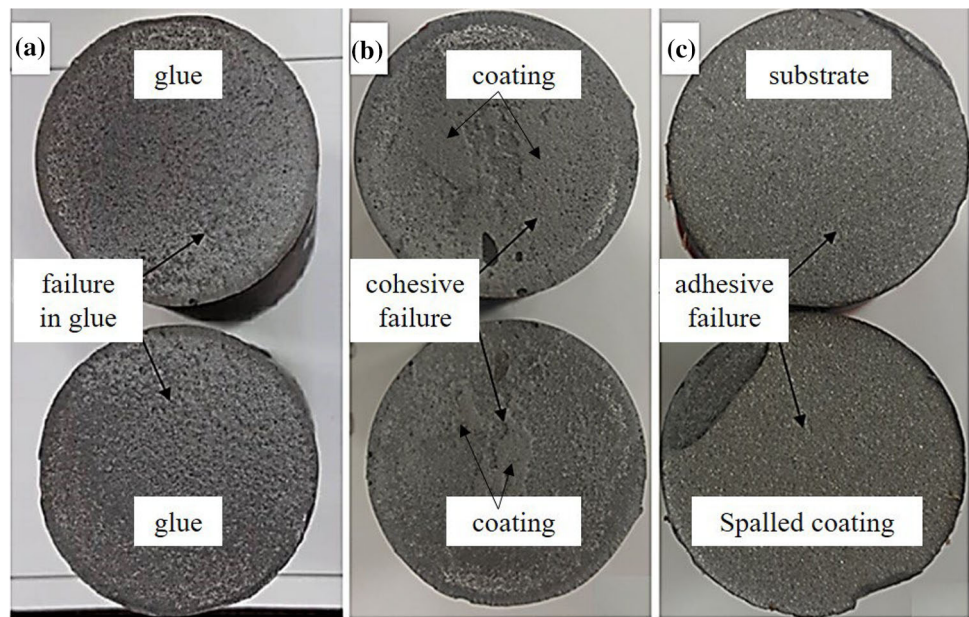
Table 4 Vickers microhardness ($HV_{0.3}$) on the polished cross section of the chromium carbide, Stellite-6 and FSX 414 hardfacing coatings

Sample	Trial 1	2	3	4	5	7	Avg. $HV_{0.3}$
Cr_3C_2-25wt%NiCr	809	1073	865	875	1046	966	939±97
Stellite-6	629	698	600	421	657	562	610 ± 98
FSX 414	762	721	804	784	741	762	760 ± 27

respectively. The scattering of the microhardness data was due to the presence of different phases in the coating structure. For example, in the case of the carbide-based coating, as described in the microscopy and phase analysis of the coating structure, the coating contained various phases including Cr_3C_2 (the hard phase), NiCr (the soft phase) and phases containing Cr and C dissolved in NiCr, resulting in a wide range of hardness values. The hardness of the coatings resulting from thermal spraying processes depends on the intrinsic hardness of the primary powders and the microstructure of the coating.

In the literature, the hardness values for Cr_3C_2-NiCr and Stellite-6 coatings have been reported to be 850-1100 $HV_{0.3}$ and 550-630 $HV_{0.3}$, respectively, which is consistent with the data of this experiment. There is, however, no information on the FSX 414 coating for comparison. Based on the data of this experiment, it could be said that the chromium carbide coating had the highest hardness values.

Regarding the two cobalt-based coatings FSX 414 and Stellite-6, although they were almost similar in composition, the former had higher hardness values, which could be due to the presence of more oxide phases as well as higher splat flattening and denser microstructure. As observed in XRD patterns, FSX 414 coating contains α-Co(Cr), $Cr_{23}C_6$ and $CoCr_2O_4$ phases, while Stellite-6 coating includes α-Co (Cr), WC and Cr_7C_3 phases. It has been reported that

molten particles show finer grains after quenching, which increases their hardness. This could also be another reason for the observed higher hardness of the well-molten FSX 414 coating over the Stellite-6 coating.

Elastic Modulus

The mean values of the elastic modulus were calculated using Eq 1 for Cr_3C_2-NiCr, Stellite-6 and FSX 414 coatings; these were 261±35, 124±30 and 164±20 GPa, respectively. Cr_3C_2-NiCr coating had higher elastic modulus values that could be related to the high intrinsic elastic modulus of the carbide phase. Compared to the Stellite-6 coating, the FSX 414 coating revealed higher values of the mechanical properties, which could be attributed to its microstructure characteristic including fewer pores and the presence of oxide phase in the form of stringers.

The elastic modulus of thermal spray coatings was not similar to that of the bulk material due to the unique and non-uniform microstructure of the coating. For example, the elastic modulus for the Stellite-6 bulk material was reported to be 237 GPa (Ref 33). The elastic modulus was strongly dependent on the microstructure, particularly on the porosity and the contact between the splats. Smaller pores and larger contact surfaces between the coating constituents led to mechanical properties close to those of the bulk material.

Table 5 Summary of the results obtained from experiments on the Cr_3C_2-25wt%NiCr, Stellite-6 and FSX 414 hardfacing coatings deposited by HVOF spraying process

| coating Features	Cr_3C_2-NiCr	Stellite-6	FSX 414
The main microstructural defect	Carbide dissolution	Unmelted particles	Oxide stringers
Phase composition	Ni(Cr), Cr_3C_2, Cr_7C_3	α-Co (Cr), WC, Cr_7C_3	α-Co(Cr), $Cr_{23}C_6$, $CoCr_2O_4$
Surface roughness: R_a (μm)	4.1	6.8	5.3
Porosity (Vol. %)	0.9	2	0.5
Tensile bond strength (MPa)	70<	54	59
Microhardness ($HV_{0.3}$)	939	610	760
Elastic modulus (GPa)	261	124	164
Volume losses after self-mated fretting wear test at 25 °C (mm^3)/ Wear mechanisms	8.15 polishing, abrasion	2.06 plastic deformation, fatigue	3.53 plastic deformation, abrasion
Volume losses after self-mated fretting wear test at 550 °C (mm^3)/ Wear mechanisms	1.16 plastic deformation and oxidation	1.51 plastic deformation and oxidation	2.64 plastic deformation and oxidation

The results of the experiments performed on Cr_3C_2-NiCr, Stellite-6 and FSX 414 coatings are represented in Table 5 for comparison. In the Cr_3C_2-NiCr coating, the dissolution of Cr_3C_2 carbide phases in the NiCr alloy was observed, which had a significant effect on the coating hardness due to the reduction of the hard phase in the coating. Stellite-6 coatings showed a relatively high content of unmelted particles, causing the observed lower bonding strength. The FSX 414 coating also showed a high amount of oxide stringers in its structure, leading to the observed increase in its hardness.
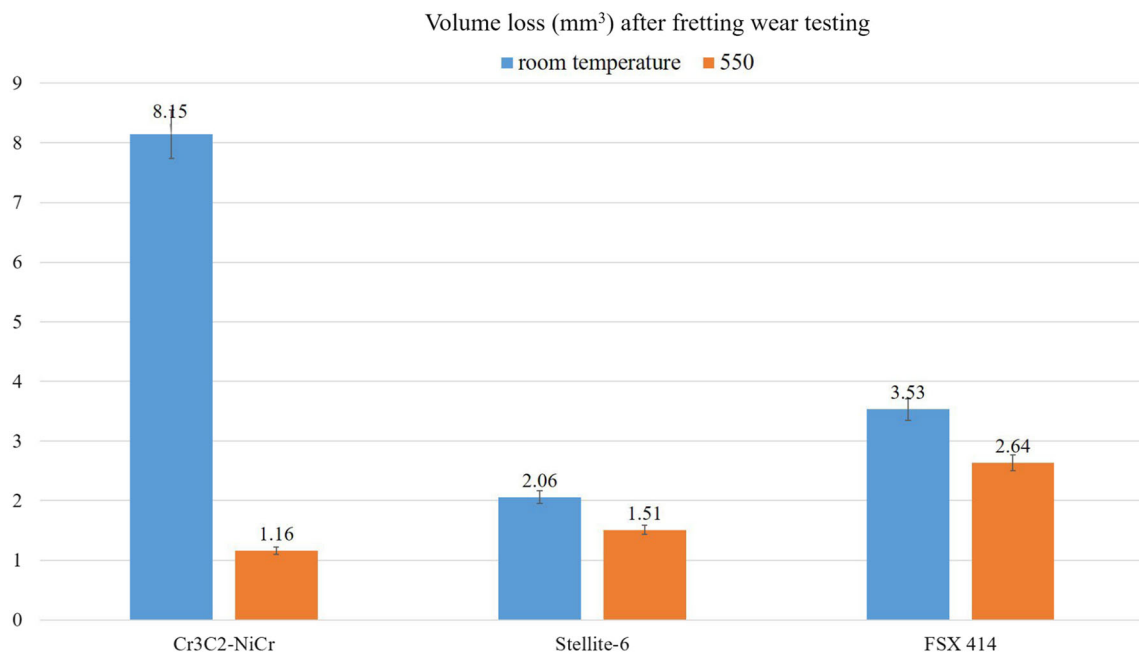
Fretting Wear Test Results

Fretting wear tests were performed on the Cr_3C_2-NiCr, Stellite-6 and FSX 414 hardfacing coatings under conditions presented in Table 3. After the wear test at room temperature (RT), the most damage was observed on the Cr_3C_2-NiCr coating and at 550 °C, discoloration was observed in all three coatings, which is most probably due to oxidation. At the high temperature, the most destructive effects were observed on the FSX414 sample. Figure 10 shows the EDS spectra of the FSX 414 worn surfaces after wear testing. As can be seen, the oxygen peak intensity after the test at 550 °C has increased compared to RM, which confirms the occurrence of oxidation in the coating.

The average volume loss values for the Cr_3C_2-NiCr, Stellite-6 and FSX 414 coatings at RT and 550 °C are given in Fig. 11. At RT, the best fretting wear resistance was related to the Stellite-6 coating and the worst performance was related to the Cr_3C_2-NiCr coating. At 550 °C, the best wear resistance was related to the Cr_3C_2-NiCr coating and the worst wear resistance was related to the FSX414 coating. All three coatings showed better wear resistance at 550 °C than at RT, especially in the case of Cr_3C_2-NiCr coating, which decreased seven times its volume loss at 550 °C.

FESEM images are taken from the surface of the coatings after spraying and after fretting wear testing at RT and 550 °C in Fig. 12, 13 and 14 in two magnifications of 200 and 1000 X. Figure 12a, 13a and 14a shows the surface morphology of the Cr_3C_2-NiCr, Stellite-6 and FSX 414 coatings after HVOF spraying of final quenched layer. This layer consists of splats and partially melted particles that have been deposited on the surface with varying degrees of flattening, leading to surface roughness. The differences in the surface morphology of the coatings at higher magnifications (10d, 11d and 12d) are clear. The Stellite-6 coating has the most and the Cr_3C_2-NiCr coating has the least unmelted particles. These observations are consistent with the measured values of surface roughness (Cr_3C_2-NiCr: 4.1, Stellite-6: 5.6 and FSX 414: 6.3 μm). It has been reported that in fretting wear, a reduction in roughness does
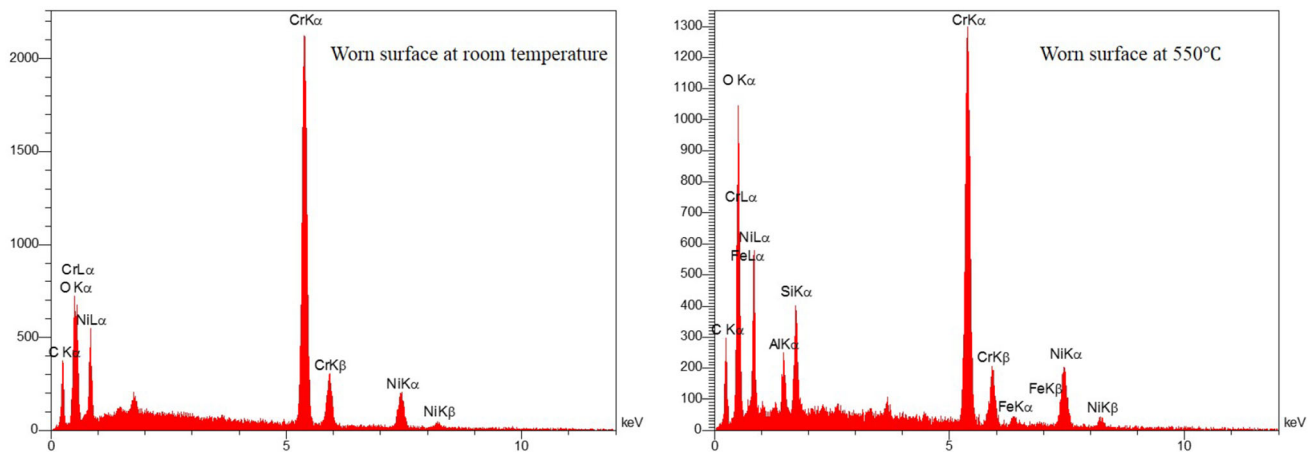
Fig. 10 EDS analysis of the FSX 414 worn surfaces after fretting wear testing at room temperature and 550 °C


Fig. 11 Average of volume loss values of the hardfacing coatings after fretting wear test at room temperature and 550 °C

not necessarily lead to a reduction in wear rate. The presence of asperities in the surface can trap wear debris and prevent the activation of the abrasive mechanism (Ref 34, 35). In the present work, the fretting wear test was done on the as-deposited coatings with the primary roughness. Investigating the effect of roughness and grinding treatment on fretting behavior is suggested as a research field.

Figure 12(b), (e) shows the Cr_3C_2-NiCr worn surface after wear test at RT. The polishing wear mechanism is observed on the coating surface. Typical wear mechanisms of HVOF hardfacing coatings are preferential wear of the NiCr phase, followed by decreasing cohesion between NiCr and Cr_3C_2 and the final detaching of carbide particles (Ref 36).

The microscopic image of the cross section of the as-sprayed Cr_3C_2-NiCr coating in Fig. 4(b) shows the primary agglomerated and sintered carbide particles in the dimensions of 1-3 μm. These particles are released from the metal matrix during fretting wear and leads to surface polishing. EDS analysis of the worn surface showed that the amount of oxygen reached 8 wt.% for the coating after the wear test at RT. Although some frictional heat can be generated in the tribo-system, no significant oxidation has occurred. At RT, in the competition between the plastic deformation of the metal phase and its destruction by carbides, the second effect is predominant. As a result, the coating experiences great volume loss during wear (8.15 mm³). The wear mechanism, observed by FESEM, is
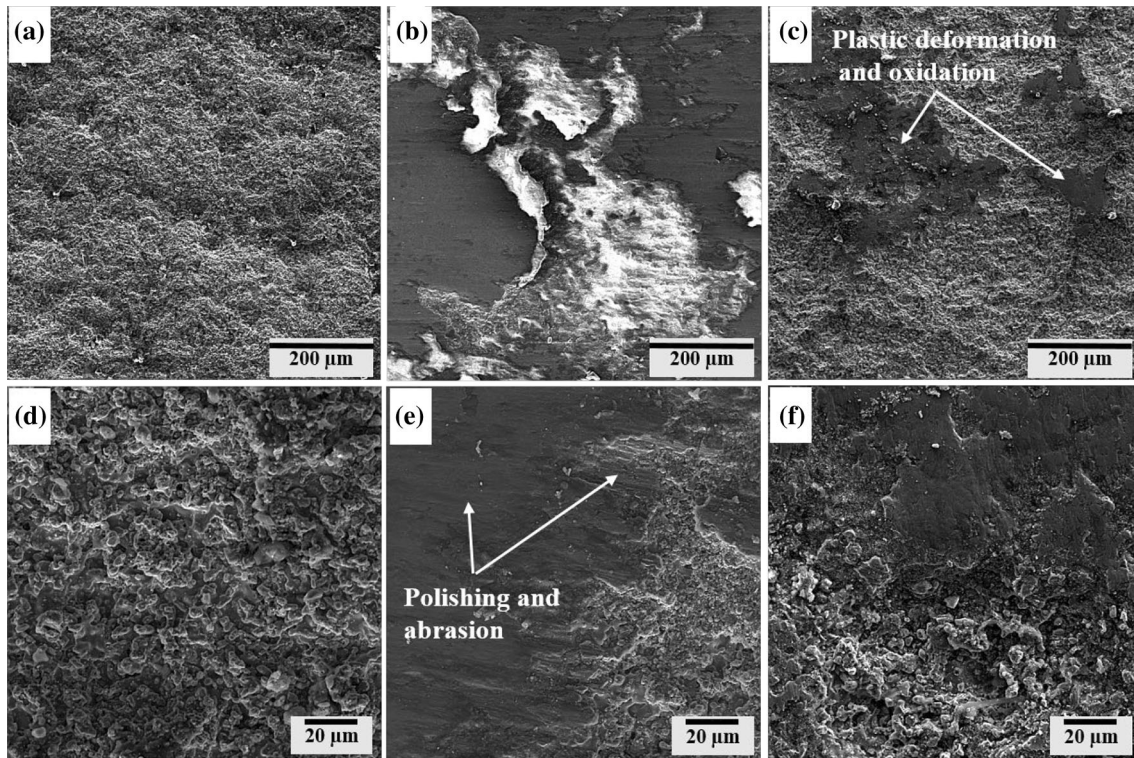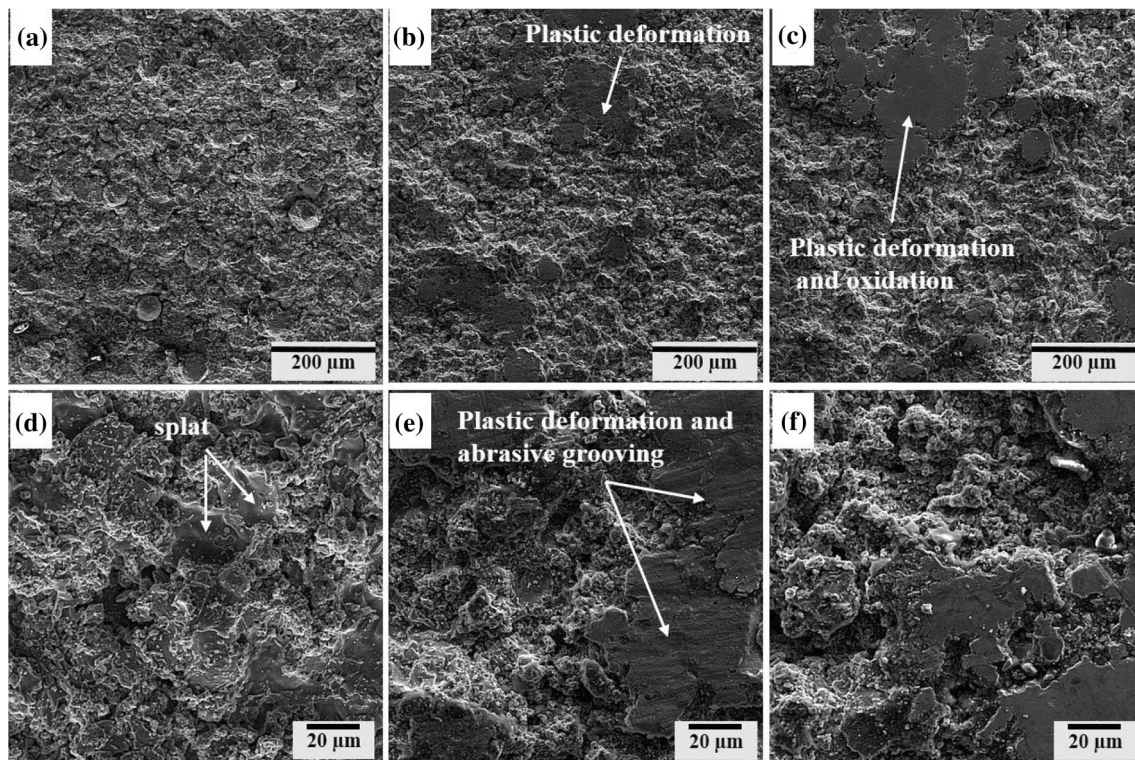
Fig. 12 FESEM images from as-sprayed (a, d) and worn surface of the Cr_3C_2-25wt%NiCr coating after fretting wear testing at room temperature (b, e) and 550 °C (c, f)
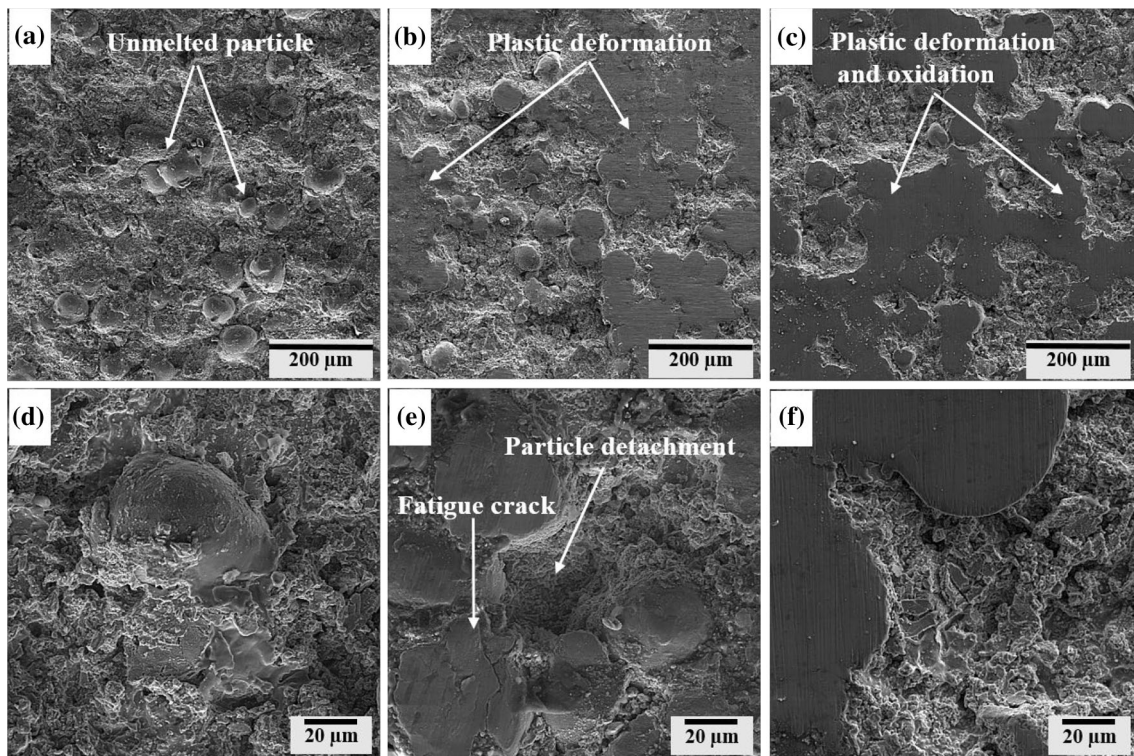
Fig. 13 FESEM images from as-sprayed (a, d) and worn surface of the Stellite-6 coating after fretting wear testing at room temperature (b, e) and 550 °C (c, f)

Fig. 14 FESEM images from as-sprayed (a, d) and worn surface of the FSX 414 coating after fretting wear testing at room temperature (b, e) and 550 °C (c, f)

shown in Fig. 12(e). The abrasion of the Cr_3C_2–NiCr coating in the fretting wear experiment happens in two stages. First, the wear of the NiCr binder causes carbide particles to come into contact. Second, the elimination of carbides occurs by fracturing or detaching by abrasive particles. Consequently, improving the NiCr hardness and Cr_3C_2 to NiCr cohesive strength may increase the fretting wear resistance of the Cr_3C_2-NiCr coating (Ref 37, 38). The FESEM image of the Cr_3C_2-NiCr coating after wear test at 550 °C (Fig. 12 c, f) shows that a sticky tribo-film with a large plastic deformation is present on the surface. This tribo-film has an oxide nature with 19.7 wt.% O_2 according to the EDS analysis. The reason for the volume loss reduction by seven times in comparison with testing at RT is the presence of the protective tribo-film, which prevents contact between the two surfaces and increases the wear resistance of the coating at high temperatures by creating a lubricating effect. Therefore, the predominant mechanism of damage to the Cr_3C_2-NiCr coating at 550 °C is plastic deformation and oxidation.

Figure 13(b), (e) shows the worn surface of the Stellite-6 coating after the wear test at RT. Some plastic deformation has occurred on the surface of the coating, especially on unmelted particles. Splats that have undergone more plastic deformation have failed. Fatigue cracks are observed on some splats (Fig. 13e). Unmelted particles also detached

from the coating surface. The amount of oxygen was measured at 6.7 wt.%, which is not much different from the amount of oxygen in the as-sprayed coating (5.5 wt.%). Therefore, Fig. 13(e) displays that the crack nucleation/propagation might have been developed at the plastically deformed splats under fatigue cycles, and most likely, detachment of splats occurs under shear fracture. It is necessary to mention that under fretting wear, cracks can propagate below the surface, especially along splat boundaries, as they are the weakest region and result in the detachment of splats at the contact surfaces. Figure 13(c), (f) shows the images of wear after testing at 550 °C, which show more plastic deformation and oxidation on the coating surface compared to wear at RT. The oxygen content was measured to be 14.1 wt.%. Unlike at RT, the worn surfaces formed at 550 °C can be characterized by oxide film as also proved by the evidence of strong oxygen peaks on the corresponding EDS spectrum. The oxide films can restrict the material transfer and adhesion wear activation. Motallebzadeh et al. (Ref 39) have found that a Stellite-12 coating at 500 °C favored CoO formation at the contact surface caused by reaction of oxygen with the Co element in the matrix.

Figure 14(b), (e) shows the worn surface of the FSX 414 coating after the wear test at RT. Plastic deformation and abrasion are observed on the wear surface. The reason for the abrasive wear is the presence of many oxides in the
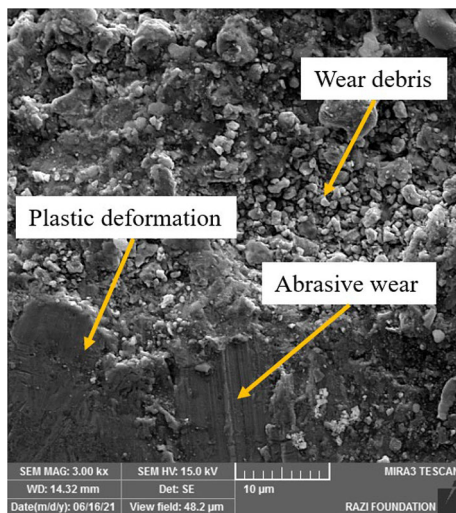
Fig. 15 FESEM image from the worn surface of the FSX 414 coating after fretting wear testing at room temperature showing wear debris, plastic deformation and abrasion

microstructure of the coating after spraying, which was discussed in the microstructure analysis of the coating. The amount of oxygen after the fretting wear test at RT was 9.5 wt.%. The reason for the greater volume loss of the FSX 414 coating than Stellite-6 is probably due to the activation of the abrasive mechanism due to the presence of oxides in its microstructure. The mentioned wear mechanisms are shown in Fig. 15. Figure 14(c), (f) shows plastic deformation and oxidation on the FSX 414 worn surface after testing at 550 °C. Unlike RT, the abrasive mechanism is not observed at the high temperature, which may be due to the activation of the plastic deformation mechanism at higher temperatures. The amount of oxygen on the coating surface measured after testing at 550 °C was about 25 wt.%. The fretting wear test results are summarized in Table 5.

To better understand the tribological behavior of the coatings, it is recommended to study the coefficient of friction behavior. The present device could not determine the coefficient of friction. Based on the results of the present study, it can be concluded that Cr_3C_2-NiCr coating deposited by HVOF process provides the most protection for gas turbine components exposed to high-temperature fretting wear.

Conclusions

The purpose of the present study was to characterize the Cr_3C_2-25 wt.% NiCr, Stellite-6 and FSX 414 hardfacing coatings. A fretting wear test was performed on the coatings at temperatures of 25 and 550 °C. The following conclusions can be drawn based on the experimental results:

- The main microstructural defects of the Cr_3C_2-NiCr, Stellite-6 and FSX 414 coatings were carbide dissolution, unmelted particles and oxide stringers, respectively. The main crystalline phases detected in the Cr_3C_2-NiCr coating were Ni (Cr) solid solution and Cr_3C_2 and Cr_7C_3 carbides. The Stellite-6 coating was composed of α-Co (Cr) solid solution and WC and Cr_7C_3 carbides. α-Co (Cr) solid solution, $Cr_{23}C_6$ and $CoCr_2O_4$ were identified in the FSX 414 coating.
- The average tensile bond strength values of Cr_3C_2-NiCr, Stellite-6 and FSX 414 coatings were more than 70, 54 and 59 MPa, respectively. The average Vickers microhardness values of Cr_3C_2-NiCr, Stellite-6 and FSX 414 coatings were 939, 610 and 760 $HV_{0.3}$, respectively. The average values of the elastic modulus of Cr_3C_2-NiCr, Stellite-6 and FSX 414 coatings were calculated to be 261, 124 and 164 GPa, respectively.
- According to the fretting wear test, Cr_3C_2-NiCr coating showed the best wear resistance at 550 °C. By contrast, the Stellite-6 coating was resisted for a longer period at RT than two other coatings. For all samples, the volume losses at 550 °C were less than at RT.
- The mechanisms of fretting wear of the Cr_3C_2-NiCr coating were polishing and abrasion at RT and plastic deformation and oxidation at 550 °C. The Co-based Stellite-6 and FSX 414 coatings exhibited plastic deformation, fatigue and abrasion at RT and plastic deformation and oxidation mechanisms at 550 °C.

References

1. "Standard Terminology Relating to Wear and Erosion," G40-13, ASTM International, 2015, p 1-9
2. P.J. Golden, Development of A Dovetail Fretting Fatigue For Turbine Engine Materials, *Int. J. Fatigue*, 2009, **31**, p 620-628. (in English)
3. C. Paulin, S. Fouvry and S. Deyber, Wear Kinetics of Ti-6Al-4V under Constant and Variable Fretting Sliding Conditions, *Wear*, 2005, **259**, p 292-299. (in English)
4. R. Rajendran, Gas Turbine Coatings (An Overview), *Eng. Fail. Anal.*, 2012, **26**, p 355-369. (in English)
5. H. Koiprasert, S. Dumrongrattana and P. Niranatlumpong, Thermally Sprayed Coatings for Protection of Fretting Wear in Land-Based Gas-Turbine Engine, *Wear*, 2004, **257**, p 1-7. (in English)
6. Y. Liu, W. Liu, Y. Ma, S. Meng, C. Liu and L. Long, A comparative study on wear and corrosion behavior of HVOF-and HVAF-sprayed WC–10Co–4Cr coatings, *Surf Eng.*, 2017, **33**, p 63-71. (in English)
7. M. Oksa, E. Turunen, T. Suhonen, T. Varis and S.P. Hannula, Optimization and Characterization of High Velocity Oxy-fuel Sprayed Coatings: Techniques, *Mater. Appl. Coat*, 2011, **1**, p 17-52. (in English)

8. A.S.M. Ang, H. Howse, S.A. Wade and C.C. Berndt, manufacturing of nickel based cermet coatings by the HVOF process, *Surf Eng.*, 2016, **32**, p 713-724. (in English)

9. D. Ghosh and S.K. Mitra, Plasma sprayed Cr_3C_2–Ni–Cr coating for oxidation protection of 2·25Cr–1Mo steel, *Surf. Eng.*, 2015, **31**(5), p 342-348. (in English)

10. V. Chaudhry and S.V. Kailas, Fretting Studies on Self-Mated Stainless Steel and Chromium Carbide Coated Surfaces under Controlled Environment Conditions, *Wear*, 2013, **301**, p 524-539. (in English)

11. E.J. Carrasquero, J. Lesage, E.S. Puchi-Cabrera and M.H. Staia, Fretting Wear of HVOF Ni–Cr Based Alloy Deposited on SAE 1045 Steel, *Surf. Coat. Technol.*, 2008, **202**(18), p 4544-4551. (in English)

12. H. Singh, T.S. Sidhu, J. Karthikeyan and S.B.S. Kalsi, Development and characterization of Cr_3C_2–NiCr coated superalloy by novel cold spray process, *Mater. Manuf. Process.*, 2016, **31**, p 1476-1482. (in English)

13. P. Sassatelli, G. Bolelli, M.L. Gualtieri and E. Heinonen, Properties of HVOF-Sprayed Stellite-6 Coatings, *Surf. Coat. Technol.*, 2018, **338**, p 45-62. (in English)

14. S.A.A. Dilawary, A. Motallebzadeh, R. Akhter, E. Atar and H. Cimenoglu, Enhanced wear resistance of Stellite 12 by Mo addition and LSM, *Surf. Eng.*, 2018, **34**, p 569-576. (in English)

15. C. Navas, A. Conde, M. Cadenas and J. De Damborenea, Tribological properties of laser clad Stellite 6 coatings on steel substrates, *Surf. Eng.*, 2006, **22**, p 26-34. (in English)

16. N. Cinca and J.M. Guilemany, Cold Gas Sprayed Stellite-6 Coatings and Their Wear Resistance, *Mater. Sci. Eng.*, 2013, **2**, p 100-122. (in English)

17. M.S. Sawant and N.K. Jain, Evaluation of stellite coatings by μ-PTA powder, laser, and PTA deposition processes, *Mater. Manuf. Process.*, 2018, **33**, p 1043-1050. (in English)

18. D.L. Oates, Microstructural Changes as a Time Temperature Indicator in Cobalt Superalloys and a NiCoCrAlTaY Coating, Ph. D. Thesis, Loughborough University, 2007.

19. S. Deshpande, A. Kulkarni, S. Sampath and H. Herman, Application of image analysis for characterization of porosity in thermal spray coatings and correlation with small angle neutron scattering, *Surf. Coat. Technol.*, 2004, **187**(1), p 6-16. (in English)

20. M. Roy, A. Pauschitz, J. Bernardi, T. Koch and F. Franek, Microstructure and Mechanical Properties of HVOF Sprayed Nanocrystalline Cr_3C_2-25(Ni20Cr) Coating, *J. Therm. Spray. Techn.*, 2006, **15**, p 372-381. (in English)

21. S.T. Aruna, N. Balaji, J. Shedthi and V.K.W. Grips, Effect of Critical Plasma Spray Parameters on the Microstructure, Microhardness and Wear and Corrosion Resistance of Plasma Sprayed Alumina Coatings, *Surf. Coat. Technol.*, 2012, **208**, p 92-100. (in English)

22. O. Vingsbo and S. Söderberg, on fretting maps, *Wear*, 1988, **126**, p 131-147. (in English)

23. L. Pawlowski, the Science and Engineering of Thermal Spray Coatings, Wiley, (2008).

24. P.L. Fauchais, J.V.R. Heberlein, M.I. Boulos, *Thermal Spray Fundamentals: From Powder to Part*, Springer Science and Business Media, 2014.

25. S. Matthews, Carbide Dissolution/Carbon Loss as a Function of Spray Distance in Unshrouded/Shrouded Plasma Sprayed Cr_3C_2-NiCr Coatings, *J. Therm. Spray. Techn.*, 2015, **24**, p 552-569. (in English)

26. S. Matthews, A. Asadov, S. Ruddell and L.M. Berger, Thermally Induced Metallurgical Processes in Cr_3C_2-NiCr Thermal Spray Coatings as a Function of Carbide Dissolution, *J. Alloy. Compd.*, 2017, **728**, p 445-463. (in English)

27. Y. Ning, P.C. Patnaik, R. Liu, M.X. Yao and X.J. Wu, Effects of Fabrication Process and Coating of Reinforcements on the Microstructure and Wear Performance of Stellite Alloy Composites, *Mater. Sci. Eng. A.*, 2005, **391**, p 313-324. (in English)

28. H.J. Kim, S.Y. Hwang, C.H. Lee and P. Juvanon, Assessment of Wear Performance of Flame Sprayed and Fused Ni-Based Coatings, *Surf. Coat. Technol.*, 2003, **172**, p 262-269. (in English)

29. S. Zimmermann, H. Kreye, Chromium carbide coatings produced with various HVOF spray systems, *ITSC 1996,* Oct 7, ASM International, 1996, pp. 147-152

30. S. Matthews, M. Hyland and B. James, Microhardness Variation in Relation to Carbide Development in Heat Treated Cr_3C_2–NiCr Thermal Spray Coatings, *Acta Mater.*, 2003, **51**, p 4267-4277. (in English)

31. M. Taheri, Z. Valefi and K. Zangeneh-Madar, Influence of HVOF process parameters on microstructure and bond strength of NiCrAlY coatings, *Surf. Eng.*, 2012, **28**, p 266-272. (in English)

32. J. Archard, Contact and Rubbing of Flat Surface, *J. Appl. Phys.*, 1953, **24**, p 981-988. (in English)

33. http://specialmetals.ir/images/technical_info/cobalt_base/Stellite_6.pdf, 2015, Accessed February 2015

34. Y. Fu, J. Wei and A.W. Batchelor, Some considerations on the mitigation of fretting damage by the application of surface-modification technologies, *J. Mat. Proc. Technol.*, 2000, **99**, p 231-245. (in English)

35. Z. Ren, F. Lai, S. Qu, Y. Zhang, X. Li and C. Yang, Effect of ultrasonic surface rolling on surface layer properties and fretting wear properties of titanium alloy Ti5Al4Mo6V2Nb1Fe, *Surf. Coat. Technol.*, 2020, **389**, 125612. (in English)

36. A.G. Bulnes, V.A. Fuentes and I.G. Cano, Understanding the Influence of High Velocity Thermal Spray Techniques on the Properties of Different Anti-Wear WC-Based Coatings, *Coatings*, 2020, **10**, p 1157. (in English)

37. G.C. Ji, C.J. Li, Y.Y. Wang and W.Y. Li, Microstructural characterization and abrasive wear performance of HVOF sprayed Cr_3C_2–NiCr coating, *Surf. Coat. Technol.*, 2006, **200**, p 6749–6757. (in English)

38. H.L. Yao, C. Yang, D.L. Yi, M.X. Zhang and H.T. Wang, Microstructure and mechanical property of high velocity oxy-fuel sprayed WC-Cr_3C_2-Ni coatings, *Surf. Coat. Technol.*, 2020, **397**, 126010. (in English)

39. A. Motallebzadeh, E. Atar and H. Cimenoglu, Sliding wear characteristics of molybdenum containing Stellite 12 coating at elevated temperatures, *Tribol. Int.*, 2015, **91**, p 40-47. (in English)